

¹⁷O NMR chemical shifts in oxometalates: from the simplest monometallic species to mixed-metal polyoxometalates†

Cite this: *Chem. Sci.*, 2014, 5, 2031Magda Pascual-Borràs,^a Xavier López,^{*a} Antonio Rodríguez-Forteza,^a
R. John Errington^b and Josep M. Poble^{*a}

We report a theoretical analysis on ¹⁷O NMR chemical shifts for a family of prototypical polyoxometalate anions. The huge diversity of structures and compositions in this family of oxometalates provides a unique resource for evaluating the influence of the metal type and connectivity over the resonance of ¹⁷O nuclei. For a set of 75 signals, we show that DFT calculations performed with the GGA-type OPBE functional, including spin-orbit and scaling corrections, provide a mean absolute error <30 ppm, a small value considering that the range of $\delta(^{17}\text{O})$ values in these systems is ~1200 ppm. For terminal M=O oxygens, the chemical shifts primarily depend on the energy gap between $\pi_{\text{M-O}}^*$ and $\sigma_{\text{M-O}}$ orbitals. When M is in its highest oxidation state, the energy of $\pi_{\text{M-O}}^*$ increases as we replace M going to the left and down in the periodic table. Consequently, we must expect large energy gaps and upfield shifts for O atoms linked to more electropositive ions. Although there is not a direct relationship between $\delta(^{17}\text{O})$ and the negative charge of the oxygen, it is not entirely wrong to correlate atomic charge and chemical shift because the ionicity of the M–O bond, the orbital energy gap and the charge density of oxygen are related. The ¹⁷O NMR chemical shifts move upfield with an increasing number of bound metal ions because of the larger energy gap in the involved orbitals. Finally, we explored the effect of protonation on $\delta(^{17}\text{O})$ in oxometalates and demonstrated that ¹⁷O NMR can be a powerful tool to identify the site(s) of protonation at low pH.

Received 9th January 2014
Accepted 10th February 2014

DOI: 10.1039/c4sc00083h

www.rsc.org/chemicalscience

1. Introduction

Polyoxometalates (or POMs) are discrete early transition metal oxides assembled from corner-, edge- and face-sharing [MO_x] units, with $x = 4\text{--}7$ and typically $\text{M} = \text{W}^{\text{VI}}, \text{Mo}^{\text{VI}}, \text{V}^{\text{V}}, \text{Nb}^{\text{V}}$ or Ta^{V} .^{1–7} Several polyanions made of U^{VI} ,⁸ Sb^{V} ,⁹ and $\text{Mn}^{\text{II/III}}$,¹⁰ as well as late transition metals such as Pd^{II} , Pt^{III} and Au^{III} ,^{11–16} are also known. The versatility of POMs is extraordinary; they conform a family of inorganic compounds with unmatched tunable physical and inorganic properties. From the pioneering studies on the magnetic properties of atomic nuclei, it was quickly understood that the nuclear resonance frequencies

depend on the chemical and electronic environment of the nuclei.^{17–19} This property has been used for many years and, thus, nuclear magnetic resonance (NMR) has become probably the most popular spectroscopic technique for compound characterization. Despite the fact that oxygen is one of the most important elements chemically and biologically, other nuclei such as ¹H, ¹³C, ³¹P or even ¹⁸³W have been prevalent in NMR studies of polyoxotungstates. The reasons are manifold, although the main shortcoming is the low natural abundance (0.037%) of the active $I = 5/2$ nucleus. Thus, enrichment of the sample with ¹⁷O is needed. In addition, $\delta(^{17}\text{O})$ NMR signals are problematic to determine accurately compared with ¹H or ¹³C because the nuclear quadrupolar interaction for ¹⁷O is very often much larger than the magnetic shielding interaction, thus causing significant line broadening in NMR spectra. However, recent advances in instrumentation, the extremely large chemical shift (δ) range—up to 2000 ppm—and the availability of ¹⁷O-enriched compounds have allowed an increasing use of ¹⁷O NMR spectroscopy.^{20,21} In 1965, ¹⁷O NMR was applied to the $\text{Cr}_2\text{O}_7^{2-}$ anion.^{22,23} Soon after, the ¹⁷O NMR spectra of a range of other oxometalates were obtained.^{24–26} In a systematic study of ¹⁷O NMR parameters of POM structures, Klemperer and co-workers clearly established the relationship between chemical shift and metal–oxygen bond lengths.²⁷

^aDepartament de Química Física i Inorgànica, Universitat Rovira i Virgili, Marcel·lí Domingo s/n, 43007 Tarragona, Spain. E-mail: josepmaria.poble@urv.cat; javier.lopez@urv.cat

^bSchool of Chemistry, Newcastle University, Newcastle upon Tyne, NE1 7RU, UK

† Electronic supplementary information (ESI) available: Figures: equivalence and classification of oxygen sites in hexametallate compounds; plot of calculated ¹⁷O chemical shifts vs. oxygen charges. Tables: computed and experimental ¹⁷O NMR chemical shifts for Lindqvist anions; computed chemical shifts for hexametallate anions with different computational methodologies; computed ¹⁷O chemical shifts of every oxygen position for the non-protonated, $[\text{V}_{10}\text{O}_{28}]^{6-}$, and two monoprotonated, $[\text{HV}_{10}\text{O}_{28}]^{5-}$, forms of the decavanadate anion along with oxygen labeling. See DOI: 10.1039/c4sc00083h

Modern quantum chemistry methods have always encountered more difficulties in describing systems containing transition metal atoms than simpler organic molecules, where approximate methods such as the density functional theory (DFT) have had great success from the beginning. However, the last two decades have seen the success of computational chemistry in tackling practically any physicochemical property related to POMs.²⁸ Quantum chemistry calculations of NMR properties in POMs started around 2000 with the study of $\delta(^{183}\text{W})$ in several typical structures, though with rather poor accuracy.²⁹ Increasing accuracy was achieved in subsequent analyses that incorporated spin-orbit (SO) corrections, solvent effects and better geometry optimizations.^{30–33} We herein make use of previous experience in the calculation of $\delta(^{183}\text{W})$ in POMs³⁴ to calculate the best possible $\delta(^{17}\text{O})$ values for mixed-metal polyoxoanions in solution. We first made an extensive exploration of density functionals and basis sets to establish a good strategy to determine accurate values. In addition, the diversity of POMs studied provides a unique opportunity to compare δ values of nuclei bonded to different transition metals, allowing us to clearly identify and understand factors contributing to these values. In the present work we focused on two main goals. First, we applied several computational methodologies based on the DFT to predict $\delta(^{17}\text{O})$ with the best accuracy possible. Secondly, we sought to understand the dependence of $\delta(^{17}\text{O})$ in POMs on the position, connectivity, vicinal metal atoms and degree of protonation of the relevant O atoms.

2. Computational details and theoretical background

Density functional theory (DFT) calculations were performed using the ADF2010 package.³⁵ In the present work we apply a family of functionals, either GGA-type^{36–43} or hybrid.^{44–46} The latter include some % of exact Hartree-Fock exchange, which makes them more computationally demanding. The process for obtaining the ^{17}O NMR chemical shifts consists of (i) a geometry optimization step and (ii) a single-point NMR calculation, a procedure expressed throughout the text as functional_{NMR}/basis_{NMR}//functional_{OPT}/basis_{OPT}. The basis sets utilized are all-electron of triple ζ + polarization (TZP) or triple- ζ + double polarization (TZ2P) quality for all atoms with scalar relativistic corrections to the electrons *via* the zeroth-order regular approximation (ZORA).^{47–49} We also tested the results for the large QZ4P basis set. The geometry optimizations were carried out under the constraints of the maximal point group symmetry of each molecule (reported in Fig. 1) and with high numerical integration accuracy (parameter set to 6 in ADF). Since we were dealing with anionic species in solution, we applied the effects of solvent and counterions as a continuum *via* the conductor-like screening model (COSMO), with a given dielectric constant (ϵ) that induces charge polarization on a surface around the molecule.^{50,51} Taking the optimized geometry, the NMR single-point calculation is done for the target and reference (H_2O) compounds introducing spin-orbit (SO) corrections and the

GIAO method.^{52–54} The calculated chemical shift is determined as, $\delta_{\text{cal}} = \sigma_{\text{ref}} - \sigma_{\text{x}}$ where σ_{x} and σ_{ref} are the isotropic average shielding for the nucleus of the target and the reference compounds, respectively.

It is known that the fundamental quantity underpinning the phenomenon of chemical shift of a nucleus is its magnetic shielding tensor, σ . The shielding tensor of nucleus A, σ_{A} , is obtained as the second derivative of the total quantum mechanical energy E of the system with respect to the external magnetic field B_0 and the magnetic moment μ_{A} of the nucleus.⁵⁵

$$\sigma_{\text{A}} = \frac{\partial^2 E}{\partial \mu_{\text{A}} \partial B_0} \Big|_{B=\mu=0} \quad (1)$$

In general, σ can be written as the sum of the paramagnetic and the diamagnetic contributions,⁵⁶ although if the relativistic theory is taken into account, the SO contribution is further included:

$$\sigma = \sigma^{\text{d}} + \sigma^{\text{p}} + \sigma^{\text{SO}} \quad (2)$$

The diamagnetic part depends on the ground state only, while the paramagnetic shielding depends also on the excited states of the unperturbed system, expressed in terms of the virtual (unoccupied) molecular orbitals (MOs). The diamagnetic contribution for a given nucleus remains fairly constant irrespective of its chemical environment so that chemical shifts are usually dominated by the paramagnetic part. The leading contribution to σ_{p} is given by the coupling between occupied and virtual MOs due to the external field \vec{B}_0 .

$$\sigma_{\text{st}}^{\text{p}} \propto \sum_i^{\text{occ}} n_i \sum_a^{\text{N}} u_{ai} \left\langle \psi_i \left| \left[\frac{\vec{r}_N}{r_N^3} \times \vec{p} \right] \right| \psi_a \right\rangle \quad (3)$$

ψ^a and ψ^i describe virtual and occupied MOs (with occupation number n_i), respectively, r_N is the electronic position operator and \vec{p} is the electronic momentum operator. The magnitude of the coupling is given by, u_{ai} which is proportional to:

$$u_{ai} \propto - \frac{\left\langle \psi_a \left| \hat{M}_{\text{u}} \right| \psi_i \right\rangle}{2(\epsilon_i^0 - \epsilon_a^0)} \quad (4)$$

where ϵ_i^0 and ϵ_a^0 are the orbital energies of the occupied and unoccupied MOs and the integral in the numerator is the first-order magnetic coupling between them. The action of the magnetic operator \hat{M}_{u} on ψ_a is simply to work with $\hat{L}_{\text{u}}^{\text{v}}$ on each atomic orbital. Here $\hat{L}_{\text{u}}^{\text{v}}$ is the u-component of the angular momentum operator with its origin at the center \vec{R}_{v} on which χ_{v} is situated. The electron orbital angular momentum operator (L_x , L_y , L_z) acts on atomic wave functions. For example,

$$L_x |p_y\rangle = i\hbar |p_z\rangle \quad (5)$$

A significant magnetic coupling occurs when an occupied orbital localized around the atomic nucleus of interest can have considerable overlap with an empty orbital after 90° rotation about the direction of the external magnetic field.^{54,57–59} Some recent studies that put emphasis in these concepts can be found in ref. 60–62.

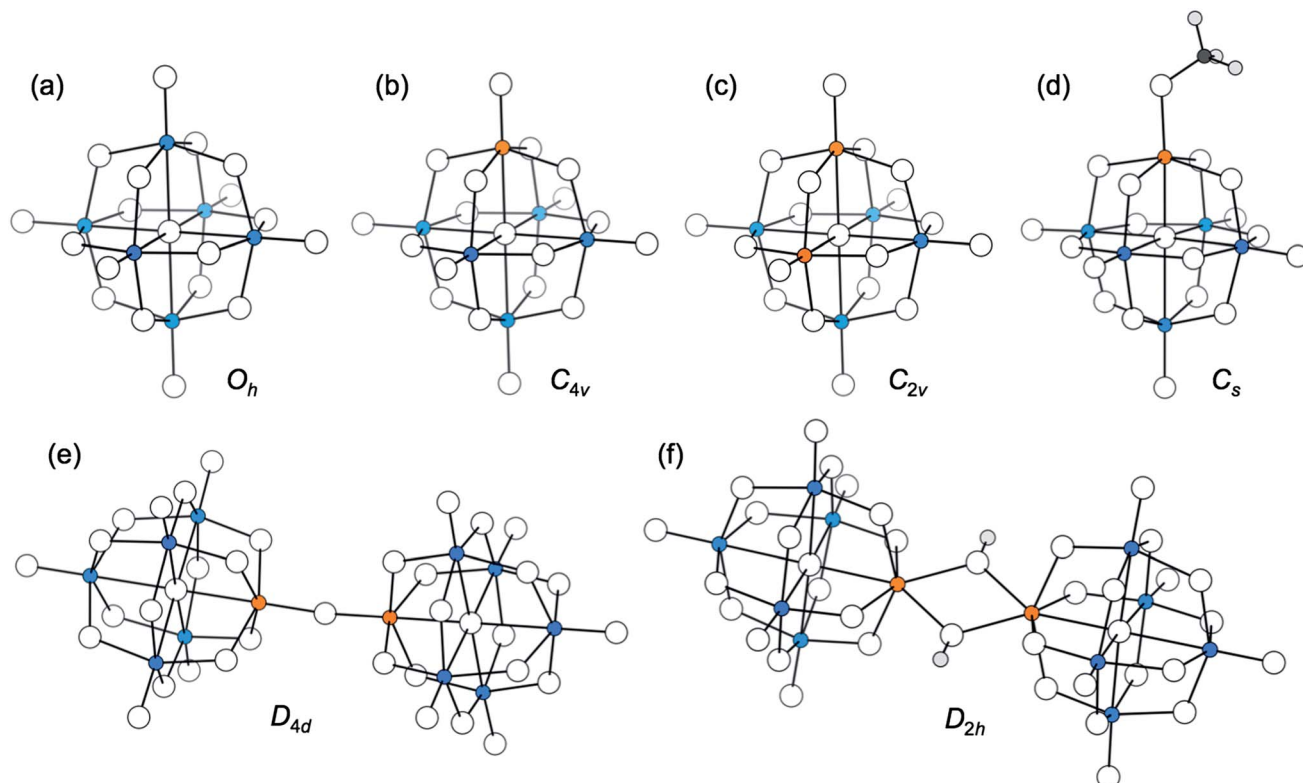


Fig. 1 Main structures analyzed, with oxygens as white spheres: (a) $[M_6O_{19}]^{n-}$, (b) $[MW_5O_{19}]^{n-}$, (c) $[M_2W_4O_{19}]^{n-}$, (d) $[(MeO)MW_5O_{18}]^{n-}$, (e) $[(\mu-O)(TiW_5O_{18})_2]^{6-}$, (f) $[\{(\mu-HO)ZrW_5O_{18}\}_2]^{6-}$. Blue atoms are W, orange are $M \neq W$. Point group symmetries are also shown.

The quality of a given calculation is referred to the mean absolute error (MAEs) either per site or as an average of them. The reported MAE values have been obtained as:

$$MAE = \frac{1}{N} \sum_i |\delta_{cal,i} - \delta_{exp,i}|$$

where $\delta_{cal,i}$ and $\delta_{exp,i}$ are the calculated and experimental chemical shifts, respectively. Fig. S1† explains how the chemical shifts for oxygens of the same type (equivalent or not) are obtained from computations.

3. Results and discussion

3.1. Calculation of accurate $\delta(^{17}O)$ for mixed-metal polyoxometalates

The family of POM structures represented in Fig. 1 has been computed and analyzed at the DFT level to provide a large set of $\delta(^{17}O)$ values. The compounds can be organized into two main groups:

(i) Single- and mixed-metal hexametalate compounds based on the Lindqvist framework, $[M_6O_{19}]^{n-}$ and $[M_{6-x}W_xO_{19}]^{n-}$. Single-metal compounds, $[M_6O_{19}]^{2-}$ (Fig. 1a), feature terminal ($M=O$), bridging (M_2O) and central (M_6O) oxygen types. The latter, internal site is weakly connected to the six M atoms. The mixed-metal derivatives $[M_xW_{6-x}O_{19}]^{n-}$ with $M = V^V, Ta^V$ or Nb^V (Fig. 1b–d), present the same three types of structural oxygen types but they can be bonded to more than one metal type, introducing additional variability to the ^{17}O NMR values.

(ii) Larger structures: dimers of the Lindqvist anion, $[(\mu-O)(TiW_5O_{18})_2]^{6-}$ and $[\{(\mu-HO)ZrW_5O_{18}\}_2]^{6-}$ (Fig. 1e–f). The Keggin, $[XW_2O_{40}]^{n-}$ ($X = P, Si$), and Wells–Dawson $[P_2W_{18}O_{62}]^{6-}$ anions also feature terminal ($M=O$) and bridging (M_2O) oxygens, plus the internal (XOM_3) sites. Fig. 2 shows the M–O connectivity modes of the POM structures presented.

Many variables affect the quality of the chemical shifts from computational techniques. A comprehensive analysis of the various sources of improvement in DFT calculations were studied for ^{99}Ru in $[Ru(CO)_3I_3]^-$.⁶³ The accurate determination is affected principally, besides the inclusion of the spin–orbit and solvent effects,⁶⁴ by the density functional and the basis set size. In the first part of this work we discuss the influence of the

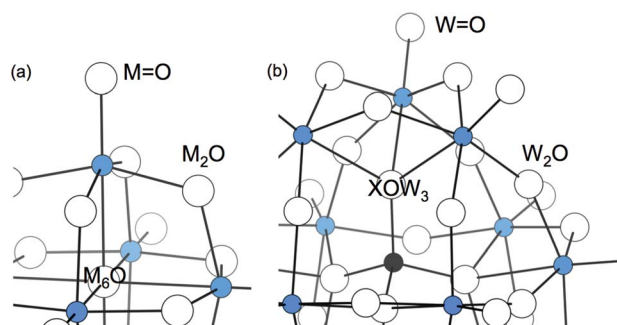


Fig. 2 Typical binding modes in (a) Lindqvist-type and (b) Wells–Dawson- and Keggin-type POMs. White spheres are oxygen atoms.

latter two on the quality of the computed ^{17}O NMR chemical shifts.

Selection of the density functional. We first focus on the effect of the density functional on the calculation of ^{17}O NMR chemical shifts. Table 1 shows a family of $\delta(^{17}\text{O})$ values computed for the simple $[\text{W}_6\text{O}_{19}]^{2-}$ structure. We carried out single-point calculations with various GGA and hybrid functionals after having optimized the geometry with the B3LYP functional and a TZP basis set. A comparison of the calculated values with the experimental ones shows that the three distinct oxygen types of $[\text{W}_6\text{O}_{19}]^{2-}$ (terminal, bridging and central) can be clearly resolved with any functional. However, there is an evident overestimation of the computed $\delta(^{17}\text{O})$, that is, they are too positive with only a few exceptions. Recent theoretical studies^{62,65} on ^{17}O NMR of terminal transition-metal oxo compounds based on DFT using ZORA show that, in general, DFT calculations reproduce the experimental chemical shifts reasonably well but the results are not within the experimental error. In the present case, the accuracy achieved is modest, as shown in the rightmost column of Table 1, with averaged MAEs ranging 40–58 ppm. The errors obtained with GGA functionals were found to be around 40–48 ppm, whereas the MAEs with hybrid functionals are ~ 10 ppm larger than GGA ones. GGA functionals perform very well for the tungsten terminal oxygen ($\text{W}=\text{O}$) whereas the error is larger for the bridging one (W_2O). Conversely, the central $\mu_6\text{-O}$ oxygen is better reproduced with hybrid functionals, probably because these are able to reproduce their special electronic properties, namely its more ionic nature, weakly bound and highly charged oxygen atom. We have observed that the GGA-type PBE and OPBE functionals perform better than the more time-consuming hybrid functionals (PBE0 and B3LYP). Previous studies testing a variety of density functional methods for small molecules also found that the OPBE performs remarkably well.^{66,67}

Effect of the basis set. The second issue to analyze is the effect of the basis set and the density functional on the geometry optimization step and, therefore, on the ^{17}O chemical shifts. We applied different combinations of these variables, as shown in Table 2, for the family of $[\text{W}_6\text{O}_{19}]^{2-}$ and $[\text{M}_2\text{W}_4\text{O}_{19}]^{4-}$ hexametalates ($\text{M} = \text{Ta}, \text{Nb}, \text{V}$) (Fig. 1a and c). The

nomenclature of the methodologies is described in the Computational details section. Thus, for instance, the PBE/TZP//B3LYP/TZ2P method consists of a geometry optimization carried out with the B3LYP functional and a TZ2P basis set, whereas the single-point calculation for the NMR values is performed with a PBE functional and a TZP basis set. The number of $\delta(^{17}\text{O})$ signals obtained with each methodology is 17 (see Tables S1–S9†), sufficiently large to give reliable information about the quality of the results. The MAEs are listed per specific oxygen type and an average of the 17 signals (rightmost column of Table 2) for each computational procedure.

First of all, we can confirm that the trends observed in Table 1 for $[\text{W}_6\text{O}_{19}]^{2-}$ are also followed in the mixed-metal compounds, namely, after using the B3LYP functional for the geometry optimization step, the single-point NMR calculation gives better results with GGA functionals than with B3LYP (entries 1, 3 and 4). In general, the NMR step gives better results with GGA functionals (PBE, OPBE). We also checked the relevance of the geometry optimization step with other functionals. Comparing entries 4 and 5 we can see what is the effect upon the total MAE of changing the geometry optimization step without changing the NMR calculation step (fixed to PBE/TZP). The MAEs do not significantly differ between B3LYP/TZ2P and PBE/TZ2P optimizations, confirming that the choice of the functional is more determinant in the NMR step than in the geometry optimization (as long as the latter is performed at least with a GGA functional and a TZP or TZ2P basis set). In addition, the difference in the average quality of the results when optimizations are performed with PBE or OPBE only differ by ~ 1 ppm, a fact showing how similar these two functionals are with respect to the geometry optimization step. Finally, the effect of the basis set in the geometry optimization step (entries 5 and 6) is residual when going from TZ2P to QZ4P. Therefore, structures optimized with a TZ2P basis set combined with the appropriate functional are good enough for NMR calculations.

To summarize, performing a test over a variety of methodologies (Table 2) shows that the best accuracy in ^{17}O NMR chemical shifts is achieved when GGA functionals are used. Except for the poor results obtained with the B3LYP/TZP//B3LYP/TZ2P procedure with an average MAE = 70 ppm, the rest of entries give much lower average MAEs, ranging 48–39 ppm. Notably, the last three methodologies in Table 2, characterized by GGA functionals, have very similar average MAEs (39–40 ppm) and, therefore, they are presumed of similar quality. For these methodologies, some positions are more accurately reproduced than others, such as $\text{W}=\text{O}$ sites (MAE between 15 and 24 ppm with this set of molecules). On the other hand, the systematic error associated with terminal $\text{M}=\text{O}$ positions is much larger (71–96 ppm), markedly influenced by the vanadium atom (*i.e.* 1015 ppm computed *vs.* 1217 ppm measured for $\text{V}=\text{O}$ in $[\text{V}_2\text{W}_4\text{O}_{19}]^{4-}$). Excluding the values for $\text{V}=\text{O}$, the $\text{M}=\text{O}$ MAE dramatically reduces. The deviations for bridging W_2O , WMO and M_2O positions are, on average, around 40 ppm. For the less chemically relevant central oxygen (M_6O), the accuracy of calculations is intermediate.

The knowledge gained from present calculations suggests that further improvement in ^{17}O NMR chemical shifts is not

Table 1 ^{17}O chemical shifts^a of the three oxygen positions of $[\text{W}_6\text{O}_{19}]^{2-}$ obtained with various functionals

Functional	δ_{calc}			MAE
	W_2O	$\text{W}=\text{O}$	W_6O	
B3LYP	500	842	−57	58
PBE0	489	841	−62	52
BP86	497	790	−30	48
PW91	498	785	−31	47
SSB-D	458	728	−30	47
PBE	490	784	−32	44
OPBE	477	759	−36	40
δ_{exp}^b	416	775	−80	

^a Values in ppm. Methods are sorted by descending MAE. The geometry was optimized with the B3LYP functional and a TZP basis set. ^b Data taken from ref. 33.

Table 2 Site-specific and average MAEs^a for the $\delta(^{17}\text{O})$ of $[\text{W}_6\text{O}_{19}]^{2-}$ and *cis*- $[\text{M}_2\text{W}_4\text{O}_{19}]^{4-}$ compounds (M = Ta, Nb, V) computed with different methodologies^b

NMR//OPT	Oxygen type						Avg.
	M ₆ O	W ₂ O	WMO	M ₂ O	W=O	M=O	
1-B3LYP/TZP//B3LYP/TZ2P	24	77	75	92	67	119	70
2-PBE/TZ2P//PBE/TZ2P	58	54	54	41	24	61	48
3-BP86/TZP//B3LYP/TZ2P	59	74	60	42	19	14	46
4-PBE/TZP//B3LYP/TZ2P	61	70	60	38	15	15	45
5-PBE/TZP//PBE/TZ2P	31	58	55	37	28	52	44
6-PBE/TZP//PBE/QZ4P	33	68	55	34	21	63	43
7-OPBE/TZP//OPBE/TZ2P	31	48	22	46	20	96	40
8-KT2/TZP//PBE/TZ2P	34	36	50	38	15	71	39
9-OPBE/TZP//PBE/TZ2P	27	40	41	41	24	76	39

^a Values in ppm. Methods are sorted by descending average MAE. The experimental data can be found in parentheses in Table 3. ^b See Tables S1–S9 for the full list of computed chemical shifts.

expected upon changes in the density functional or the basis set in the computational procedure. Also, the computed $\delta(^{17}\text{O})$ values are systematically too positive.

3.2. Linear scaling to reduce the mean absolute errors in $\delta(^{17}\text{O})$

From the results listed in Table 2, we can choose any of the last three procedures to carry on our study. However, the OPBE/TZP//PBE/TZ2P procedure (last row of Tables 2 and S9†) gives more constant deviations per site, whereas the KT2 functional has more fluctuating error values. In the following, all the values computed are referred to the OPBE/TZP//PBE/TZ2P computational procedure although one could consider using the KT2/TZP//PBE/TZ2P procedure with a comparable success.

For the chosen procedure, then, the average MAE = 39 ppm is still moderate despite the wide range of $\delta(^{17}\text{O}) \sim 1200$ ppm in POMs. At this point we consider a general approach to overcome this issue. Empirical scaling is the application of corrections to the computed data derived from linear regression procedures using experimental data.⁷² In this case, computed isotropic shieldings (σ) with the OPBE/TZP//PBE/TZ2P procedure and experimental chemical shifts (δ) are related *via* an equation of the form $\delta = b\sigma + a$. The major benefit of this analysis is that the slope (b) is a scaling factor to robustly account for the systematic errors in computed chemical shifts. This procedure is able to reduce errors from sources such as solvation effects, rovibratory effects and other methodological limitations.⁷³ Fig. 3 shows the linear equation $\delta = -1.079\sigma + 313.0$ fitting the computed ^{17}O shielding to the experimental ^{17}O chemical shifts for the set of compounds listed in Table 3. So, using that equation we can reduce the systematic errors. A slope more negative than -1 indicates that the routinely computed chemical shifts were overestimated. A second linear regression was done with the bridging oxygens only, due to their larger error compared with the other oxygen types.

The values of $\delta(^{17}\text{O})$ shown in Table 3 have been obtained with the mentioned linear equations. Notice that we have enlarged the number of compounds to which we applied the linear scaling to systems classified as (i) and (ii) in Section 3.1.

The fitted values are more accurate in general than the non-fitted ones. The two of them coincide, though, in that the most accurately computed $\delta(^{17}\text{O})$ values are those of terminal W=O oxygens. The empirical fitting also provides a quantitative accuracy for oxygens of the Keggin compound such as the internal XOM₃ position (MAE = 10 ppm). However, it does not perform so well for M₂O oxygens, maybe because the fitting includes a majority of values for W₂O oxygens. The improvement is therefore more evident for oxygens linked to W, although better results are also observed with the other metals, M. Table 4 summarizes the % improvement experienced when computed $\delta(^{17}\text{O})$ are fitted using the linear equation in Fig. 3. The systematic errors in $\delta(^{17}\text{O})$ are notably reduced applying the linear fitting technique to the values computed with the OPBE/TZP//PBE/TZ2P procedure. The oxygens bonded to W atoms feature small MAEs between 7 and 17 ppm. On the other hand, the terminal V=O site is a special case since the computed chemical shift is still large after applying such fitting correction.

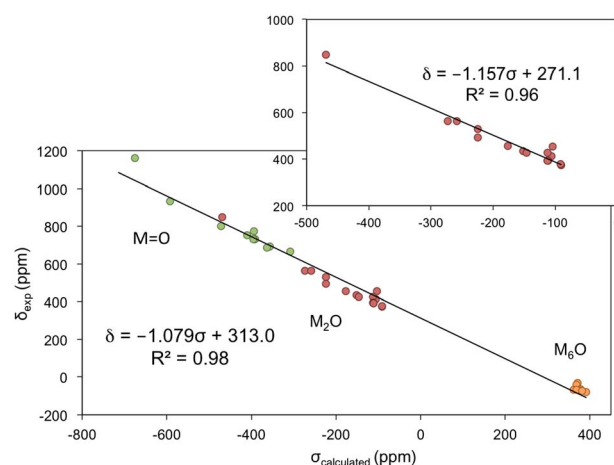


Fig. 3 Plot and linear regression of experimental chemical shifts, δ_{exp} , vs. calculated shieldings, $\sigma_{\text{calculated}}$, for the oxygen positions taken from the hexametalate compounds listed in Table S10.† Inlay contains the points and linear regression for the M₂O sites separately.

Table 3 Fitted and experimental^a ¹⁷O shifts for several polyoxotungstates^b

Anion	M ₆ O	W ₂ O	WMO	M ₂ O	W=O	M=O	XOW ₃	Ref.
[W ₆ O ₁₉] ²⁻	-109 (-80)	394 (416)	—	—	738 (775)	—	—	25
[TaW ₅ O ₁₉] ³⁻	-94 (-71)	401 (394)	440 (426)	—	737 (732)	645 (666)	—	68
[NbW ₅ O ₁₉] ³⁻	-85 (-67)	400 (393)	475 (456)	—	735 (731)	821 (799)	—	68
[VW ₅ O ₁₉] ³⁻	-99 (-75)	401 (392)	570 (562)	—	739 (731)	1083 (1217)	—	25
[Ta ₂ W ₄ O ₁₉] ³⁻	-85 (-40)	379	401	391 (454)	702	608	—	—
[Nb ₂ W ₄ O ₁₉] ⁴⁻	-78 (-67)	376 (379)	447 (435)	530 (493)	698 (691)	755 (753)	—	68
[V ₂ W ₄ O ₁₉] ⁴⁻	-95 (-65)	376 (378)	531 (530)	814 (848)	705 (687)	1042 (1162)	—	25
[(MeO)SnW ₅ O ₁₈] ³⁻	25 (17)	394; 407 (363; 383)	376 (395)	—	718; 672 (720; 684)	—	—	69
[(MeO)ZrW ₅ O ₁₈] ³⁻	-64 (-58)	387; 390 (385; 377)	478 (484)	—	719; 706 (711; 691)	—	—	70
[(MeO)TiW ₅ O ₁₈] ³⁻	-71 (-58)	387; 393 (380; 390)	534 (525)	—	723; 716 (721; 713)	—	—	71
[(μ-O)(TiW ₅ O ₁₈) ₂] ⁶⁻	-81 (-63)	389; 397 (381; 390)	545 (534)	757 (697)	725; 721 (722; 714)	—	—	71
[(μ-HO)ZrW ₅ O ₁₈] ₂ ⁶⁻	-78 (-58)	383; 393 (378; 387)	519 (479)	—	714; 703 (712; 692)	—	—	70
α-[PW ₁₂ O ₄₀] ³⁻	—	432; 456 (405; 431)	—	—	765 (769)	—	91 (80)	27
α-[SiW ₁₂ O ₄₀] ⁴⁻	—	428; 446 (405; 427)	—	—	761 (761)	—	37 (27)	27
[P ₂ W ₁₈ O ₆₂] ⁶⁻	—	435 (418)	—	—	740; 760 (738; 759)	—	75; 106	27
MAE	17	13	14	48	6	60 ^c	10	—

^a Values in parentheses. ^b Values in ppm. ^c This MAE decreases to 15 ppm if the vanadium-derived values are not considered. All the calculations were performed using CH₃CN as solvent except for [W₆O₁₉]²⁻, which was performed with DMF.

Table 4 MAEs^a for calculated and fitted $\delta(^{17}\text{O})$ for hexametalate compounds

Site	Calculated ^b	Fitted	Improvement (%)
M ₆ O	38	17	55
W ₂ O	60	13	78
WMO	44	14	68
M ₂ O	59	48	19
W=O	7	6	14
M=O ^c	69 (11)	60 (15)	13
Average ^c	46 (36)	26 (19)	44 (47)

^a Values in ppm. ^b Data in Table S1. ^c In parentheses, MAEs obtained excluding $\delta(^{17}\text{O})$ of terminal V=O sites.

3.3. Influence of the metal on the chemical shift

To help us explain the ¹⁷O NMR of complex POM systems, we firstly analyze its behavior in the simpler and well characterized MO₄ⁿ⁻ compounds, with M of groups 5, 6, 7 and 8 of the periodic table. These compounds were previously studied as models for the performance of theoretically methods in ¹⁷O NMR properties.⁷⁴⁻⁷⁶ Calculated and experimental $\delta(^{17}\text{O})$ values are shown in Table 5. As stated above, the chemical shifts are governed by the paramagnetic term, σ^P , which in MO₄ⁿ⁻ anions is dominated by a $np(\text{O}) \rightarrow \pi^*(\text{M}-\text{O})$ electronic transition where $np(\text{O})$ is the occupied symmetry-adapted lone pair of the oxygen atoms (lhs of Scheme 1). Recalling eqn (4), the term u_{ai} , responsible for σ^P , depends on the reciprocal of the energy gap between these two orbitals, $\Delta\epsilon^{-1}$, but also on the overlap (considering rotation due to the external magnetic field) between the oxygen atomic contributions in both orbitals.^{33,54} Fig. 4 shows that the energies of $np(\text{O})$ and π^* orbitals, defining $\Delta\epsilon^{-1}$, decrease as we go right and up in the periodic table. Interestingly, the π^* orbital does so more dramatically. This is linked to the varying M–O bond polarization towards a larger oxygen character in the same sense. However, the occupied lone

pair orbital remains constant at >95% p(O) character, its energy change being attributed to the different negative charges in the MO₄ⁿ⁻ family.

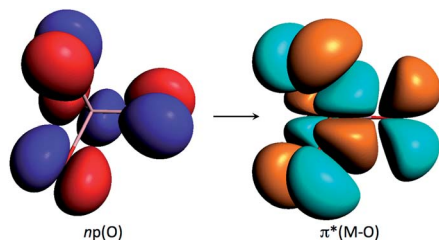
Within this series the correlation of ¹⁷O chemical shifts with the orbital gaps is highly linear, as shown in Fig. 4. When we move left and down in the periodic table, the ionicity of the metal–oxygen bond increases. After having analyzed the computational results we can conclude that the numerator of the u_{ai} term is quite irrelevant (constant) vs. the chemical shift, the energy gap being entirely responsible for the trend in $\delta(^{17}\text{O})$. Hence, for example, the contribution of p(O) to $\pi^*(\text{M}-\text{O})$ is only 35% in WO₄²⁻ whereas it reaches up to 60% in RuO₄. This might affect the numerator of u_{ai} , but it does so only slightly and the varying % p(O) contributions have little effect, apart from the indirect effect on the energy of the π^* orbital. Thus, the observed $\delta(^{17}\text{O})$ resonance in WO₄²⁻ appears at 456 ppm, whereas that for RuO₄ is shifted 700 ppm downfield to 1142 ppm. The computed values are rather close to the observed ones, 452 and 1071 ppm, respectively. The mentioned downfield shift can be attributed in simple terms to the increase of covalency in the M–O bond and to the higher electron affinity of the metal. Both effects are present in the orbital gap mentioned. Likely, many chemists would prefer an interpretation based on atomic populations. It is true that the atomic charge of oxygens

Table 5 Calculated and experimental^a ¹⁷O NMR shifts^b for MO₄ⁿ⁻

VO ₄ ³⁻	CrO ₄ ²⁻	MnO ₄ ⁻	
548 (568)	758 (871)	1030 (1255)	
NbO ₄ ³⁻	MoO ₄ ²⁻	TcO ₄ ⁻	RuO ₄
419 (—)	578 (576)	783 (786)	1071 (1142)
TaO ₄ ³⁻	WO ₄ ²⁻	ReO ₄ ⁻	OsO ₄
332 (—)	452 (456)	597 (605)	800 (832)

^a Data in parentheses from ref. 77 and 78 except for RuO₄ (ref. 79).

^b Values in ppm.



Scheme 1

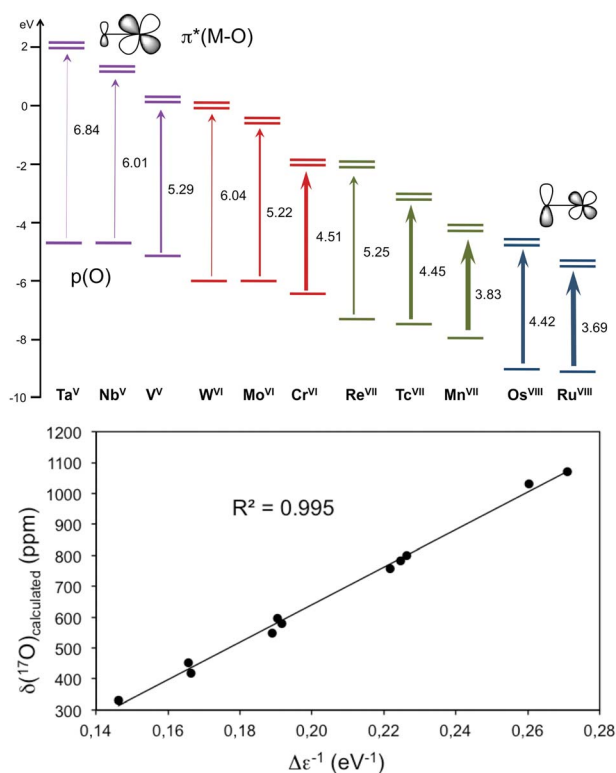


Fig. 4 Dependence of ^{17}O chemical shifts on the energy gaps associated with the leading occupied \rightarrow virtual electronic transitions in the σ^p component for the MO_4^{n-} series. Top: computed $n \rightarrow \pi^*(\text{M}-\text{O})$ energy gaps (in eV). More covalent M–O bonds are associated with smaller gaps (thicker arrows) and more deshielded nuclei. Bottom: linear correlation of the calculated $\delta(^{17}\text{O})$ vs. the reciprocal of the energy gap ($\Delta\epsilon^{-1}$).

in WO_4^{2-} is larger than in RuO_4 (-1.00e vs. -0.46e , respectively, with multipole-derived atomic charges) but the reader should take into account that $\delta(^{17}\text{O})$ correlates much better with the reciprocal of orbital energy gaps, $\Delta\epsilon^{-1}$, than with atomic populations (see Fig. S2†). Both factors—orbital energy gap and, secondarily, orbital polarization—make the $n \rightarrow \pi^*$ electron transfer less accessible in the tungstate species. A deeper analysis of the MO_4^{n-} model set shows that the behavior of $\delta(^{17}\text{O})$ can be rationalized mainly in terms of the orbital energy gap, the % contribution of p(O) in the implicated orbitals being indirect, affecting their relative energies.

The computed $\delta(^{17}\text{O})$ values fitted by the expressions shown in Fig. 3 for bridging MOW and MOM oxygens in hexametalate

anions are listed in Table 6 along with experimental values. If we consider MOW sites, the variations in the chemical shift are within the range 400–600 ppm, smaller than in MO_4^{n-} . The changes are larger if we look at the MOM sites. Notably, an increase in the covalency of M–O bonds, going up in a group, produce larger chemical shifts. In a period, though, they remain fairly constant (fitted and experimental values). Viewed as a whole, the $\delta(^{17}\text{O})$ values for hexametalate POM compounds follow the same trends as the MO_4^{n-} set. Therefore their behaviors can be assigned to the same origin.

3.4. Relevance of the bonding mode

In addition to the metal atom bonded to the oxygen site, the nature of this interaction, related to the number of vicinal metal atoms, notably affects the chemical shift. For a family of polyoxotungstates computed (Fig. 5a) it is relevant that the negative atomic charge assigned to the oxygen atom increases as $\text{WO} < \text{W}_2\text{O} < \text{W}_6\text{O}$, i.e. when more vicinal metal atoms and larger W–O distances are present. Thus, the W–O bonds become less covalent and the occupied and virtual orbitals split apart, lowering the $\delta(^{17}\text{O})$ due to a decrease in the paramagnetic contribution to σ . Within any one type of oxygen (W_2O , for example), though, one cannot find any correlation between atomic charges and the associated chemical shifts.

Regarding the M–O bond distance, it provides an indication of the nature of the bond, which is important in determining the variations in $\delta(^{17}\text{O})$. For MO_4^{n-} , we studied the main electronic transitions, but herein we focus on the relationship between V–O bond distances and $\delta(^{17}\text{O})$ in $[\text{V}_{10}\text{O}_{28}]^{6-}$ due to the increase in the number of paramagnetic transitions, which makes the analysis of orbital couplings much more intricate (Fig. 5b). We chose the decavanadate system (Fig. 7) to illustrate this trend because it contains four different V_xO oxygen types ($x = 1, 2, 3$ and 6). The relationship between energy gaps and bond distances is used to explain the trends in the $\delta(^{17}\text{O})$ in this oxovanadate. As can be seen in Fig. 5b, as the V–O bond distance increases, the nature of the interaction becomes more ionic and the chemical shift decreases.

The paramagnetic contribution is the most important source of the shielding. Therefore, we further examined the main orbital transitions dominating this contribution in $\text{M}=\text{O}$ and M_2O oxygen sites since they are the most common in POMs. In the models represented in Fig. 6, there is one dominant contribution, namely the $\sigma \rightarrow \pi^*$ magnetic coupling, in terminal $\text{M}=\text{O}$ sites, which accounts for about 40–70% of the total depending on the metal. On the other hand, the largest

Table 6 Fitted and experimental^a $\delta(^{17}\text{O})$ values^b for MOW and M_2O positions in mixed-metal hexametalates

MOW				MOM			
V	570 (562)			V	814 (848)		
Nb	475 (456)	Mo	505 (485)	Nb	530 (493)	Mo	611 (563)
Ta	440 (426)	W	394 (413)	Ta	391 (454)	W	394 (413)

^a In parentheses. ^b Values in ppm.

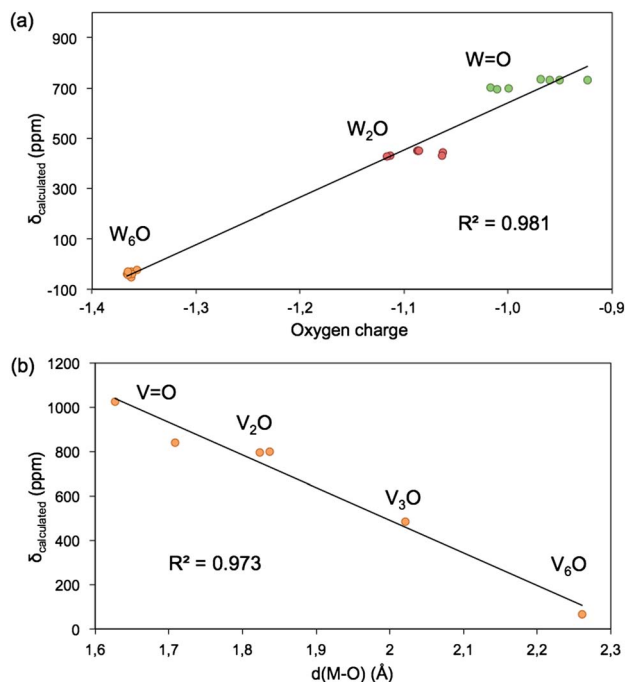


Fig. 5 Correlation of the calculated ^{17}O chemical shifts with (a) oxygen charges in substituted hexametalate anions, and with (b) V–O distances in the $[\text{V}_{10}\text{O}_{28}]^{6-}$ anion.

contribution to M_2O shifts comes from the $np(\text{O}) \rightarrow \pi^*$ coupling, which accounts for about 30% of all transitions. Fig. 6 schematically shows how if one rotates a σ or n orbital by 90° as indicated by the arrows, it overlaps with the empty π^* orbital, particularly in the region around the oxygen. As the number of metal atoms bonded to the oxygen increases, there is no single dominant transition any more, but many of them contribute to the paramagnetic term.

3.5. Effects of localised and mobile protons on the chemical shift

POMs are anionic species that can be protonated at neutral to acidic pH conditions, depending on their composition and charge. The identification of basic oxygens has significant implications regarding chemical reactivity and, more specifically, catalytic activity of metal oxides in general. However, the protonation sites in POMs are an elusive subject (i) naturally, since protons are itinerant in structures with chemically similar oxygen sites, and (ii) technically, due to the difficulties associated with the structural determination of H atom positions. Even so, in some cases, protonation sites have been determined experimentally using the empirical relationship between ‘bond length’ and ‘bond strength’.⁸⁰ In other cases, positions can be proposed based on ^{17}O NMR spectra.^{25,80–84} Computationally, this subject has been tackled by many authors.^{85–89} To analyze the effect of protonation on ^{17}O NMR of POMs, we focus on the well characterized decavanadate $[\text{V}_{10}\text{O}_{28}]^{6-}$ anion, represented in Fig. 7, since it features seven structural oxygen sites, six of which are external and could potentially be protonated. In a series of experimental studies,^{80–82} the location of protons in

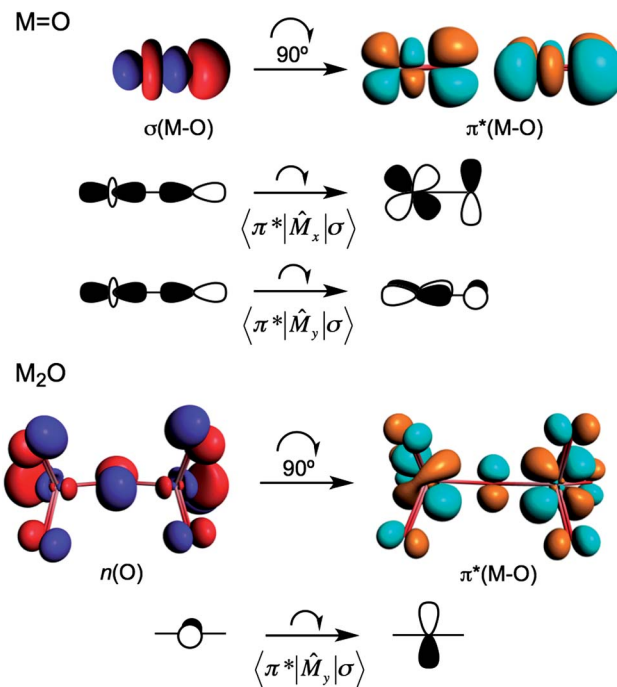


Fig. 6 Main contributions to the paramagnetic shielding for $\text{M}=\text{O}$ (top) and M_2O (bottom) oxygen types obtained with simplified models. The symbolic representation of the σ and n occupied orbitals qualitatively illustrates how the action of the magnetic field rotates the atomic orbitals by 90° .

this compound and their effect on ^{17}O NMR was analyzed. First, it must be stressed that seven signals (labeled A–G) appear in the spectrum at any pH, proving that the effective C_{2h} symmetry is preserved irrespective of the protonation state of the species due to fast proton exchange at the NMR timescale.

Second, as the solution is acidified, two NMR signals, assigned to the bridging oxygens B (OV_3) and C (OV_2), experience an upfield shift ($\Delta\delta < 0$), whereas the other oxygen signals shift downfield ($\Delta\delta > 0$) by small amounts. Terminal positions F and G ($\text{V}=\text{O}$) are not basic. A general sequence of increasing

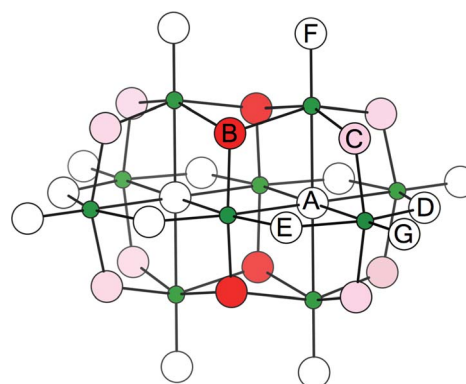


Fig. 7 The $[\text{V}_{10}\text{O}_{28}]^{6-}$ anion with labeling of one member of each set of symmetry-equivalent oxygens: (A) V_6O ; (B) V_3O ; (C–E) V_2O ; (F–G) VO . Red and pink colors identify a 60% and 40% degree of protonation in sites B and C in $[\text{HV}_{10}\text{O}_{28}]^{5-}$ (see text).

negative charge has been proposed as $O_G \sim O_F < O_E < O_D < O_C < O_B < O_A$ that can be related to their basicity.⁸⁵ Because O_A is inaccessible to protons, O_B and O_C are effectively the most basic oxygens, with O_B slightly more basic than O_C .

The main goal of our calculations was to reproduce and explain these experimental trends and to extract some general conclusions related to protonation in POMs. In general, calculations predict a huge and apparently unrealistic decrease of $\delta(^{17}\text{O})$ when a single oxygen is protonated. For $V_{10}O_{28}^{6-}$, the computed change in $\delta(^{17}\text{O})$ for the bridging OV_2 is $\Delta\delta(^{17}\text{O}) \approx -580$ ppm when protonation occurs considering the short timescale (a static protonated structure with a non-itinerant proton). In the same way, the bridging oxygens of the Lindqvist structure listed in Table 7 feature large $\Delta\delta(^{17}\text{O})$ changes. However, basic oxygens (VOV) change their $\Delta\delta(^{17}\text{O})$ more than non-basic ones, for which $\Delta\delta(^{17}\text{O})$ ranges from -300 to -400 ppm for $M = W, Nb$. Hence, the change in chemical shift associated to protonation depends on the metal atoms linked to the oxygen.

The geometrical effects of protonation might help us find an explanation for the variations in δ . The last row in Table 7 shows the change in some M–O distances if we attach a proton to a single oxygen site. It can be seen that the structural change is large, ranging from $+0.149$ Å for OW_2 to $+0.166$ Å for OV_2 at the present level of computation. Consequently, the protonated oxygens gain some ionic character and the δ moves upfield. We find that the smallest changes in chemical shift are associated with the smallest geometrical changes ($M = W$), and *vice versa* (OV_2). The geometrical changes encountered for W and V upon protonation are so similar in fact that we conjecture that the structural change is not the main reason for the wide range of 300 ppm of $\Delta\delta$ obtained. On the other hand, other M–O distances either elongate or shorten by about ± 0.05 Å on average. There is also a correlation with the initial $\delta(^{17}\text{O})$ position: the more downfield the initial value, the larger the upfield change after protonation. It is also important to mention that the neighboring oxygens of a protonated site experience a positive $\Delta\delta(^{17}\text{O})$ of several tens of ppm (Table S11†) that must be taken into consideration for the final results. These trends may seem erroneous if compared to the small changes observed by ^{17}O NMR. However, they become logical at the NMR timescale, where the itinerant character of the proton emerges. To take into account such effects, we must consider the following facts:

(1) Taking static structures, the changes in $\delta(^{17}\text{O})$ are either $\Delta\delta < 0$ for the protonated oxygen, and $\Delta\delta > 0$ for all the other non-protonated sites.

Table 7 Calculated $\delta(^{17}\text{O})$ for non-protonated and protonated metal substituted Lindqvist structures, and their difference $\Delta\delta$.^a The structural change, $\Delta d(M-O)$, is shown

	WOW	WONb	NbONb	WOV	VOV
Non-prot.	445	516	563	563	808
Protonated	152	150	171	149	237
$\Delta\delta(^{17}\text{O})$	−293	−366	−392	−414	−571
$\Delta d(M-O)^b$	+0.149		+0.159		+0.166

^a Values in ppm. ^b M–O change upon protonation, in Å.

(2) Equivalence of oxygen sites and long timescales. $[V_{10}O_{28}]^{6-}$ belongs to the C_{2h} point group, with four O_B and eight O_C equivalent sites. If symmetry must be preserved in the protonated form, the ^{17}O chemical shift of the protonated oxygen ($\Delta\delta < 0$) and its non-protonated partner sites ($\Delta\delta > 0$) will be duly averaged to take into account proton exchange between these N equivalent sites, in such a way that a unique signal is obtained for this set of sites.

(3) Coexistence of two protonated species. During the NMR measurements, more than one protonated species can be present in solution at sufficiently low pH, namely, $[V_{10}O_{28}]^{6-}$ can be protonated in oxygens B or C.

Table 8 lists the computed $\delta(^{17}\text{O})$ for the non-protonated, and the two protonated species derived from the decavanadate anion in the long timescale, along with the experimental changes in $\delta(^{17}\text{O})$. The complete list of non-averaged chemical shifts for every individual oxygen position in the two protonated species can be found in Table S3.† For each particular protonated species (columns ‘HO_B’ or ‘HO_C’), one $\delta(^{17}\text{O})$ decreases and the others increase compared to the non-protonated species. This behavior reveals that protonation does not only occur at the most basic site B but rather at both B and C sites, as their negative $\Delta\delta_{\text{exp}}$ values reveal. Column ‘60_B : 40_C’ shows the results if the two previous columns are combined as if $HV_{10}O_{28}^{5-}$ was 60% protonated in B and 40% protonated in C. We found that this balanced combination of the ^{17}O shieldings calculated for HO_B and HO_C reproduce the experimental data in the rightmost column, not only for protonated sites B and C, but also for non-protonated sites that shift downfield. Other ratios different from 60_B : 40_C provided poorer estimations when comparing with experimental shifts (Table S12†). The present procedure applied to DFT calculations proves that the observed $\delta(^{17}\text{O})$ signals are a weighted mixture of those resonances assigned to equivalent oxygen types because they undergo mutual proton exchange in the timescale of ^{17}O NMR measurements. It has also been proven that oxygen B is more basic than C since the weighted combination that matches the experiments contains a higher % of $[HV_{10}O_{28}]^{5-}$ protonated at B. Therefore, the calculated values are only comparable with experimental ones if the effects discussed above are duly combined.

Finally, the case of $V_2W_4O_{19}^{4-}/HV_2W_4O_{19}^{3-}$, that was experimentally analyzed,²⁵ revealed a change in the OV_2 site of

Table 8 Evolution of the experimental and calculated $\delta(^{17}\text{O})$ of external oxygens upon protonation

	$[V_{10}O_{28}]^{6-}$	$HV_{10}O_{28}^{5-}$			$\Delta\delta_{\text{cal}}^a$	$\Delta\delta_{\text{exp}}^b$
		HO _B	HO _C	60 _B : 40 _C		
O_B	498	433	520	468	−30	−28
O_C	785	803	734	776	−9	−7
O_D	791	814	818	816	25	23
O_E	826	830	837	833	7	11
$O_{F,G}$	1000	1020	1025	1022	22	17

^a $\Delta\delta_{\text{cal}} = \delta(^{17}\text{O}, 60_B : 40_C) - \delta(^{17}\text{O}, V_{10}O_{28}^{6-})$. See text for details. ^b $\Delta\delta_{\text{exp}} = \delta(^{17}\text{O}, \text{pH } 4.5) - \delta(^{17}\text{O}, \text{pH } 6)$. Data taken from ref. 80.

–238 ppm upon protonation. Dramatic changes in $\delta(^{17}\text{O})$ shifts were also detected and computed for various amide types.⁹⁰ Although it is much larger than $\Delta\delta = -7$ ppm obtained for the chemically similar O_C in the decavanadate anion, it is still much smaller than our predicted value of $\Delta\delta = -571$ ppm (Table 7). As described in this section, a small change in $\delta(^{17}\text{O})$ when protonation occurs can be explained by proton delocalization over other equivalent or non-equivalent oxygen sites. In the case of $[\text{V}_2\text{W}_4\text{O}_{19}]^{4-}$, the absence of other similarly basic (equivalent or non-equivalent) sites discards the possibility of dissipation of $\Delta\delta$ by proton delocalization. As a matter of fact, there is a lone OV_2 position, and WOV sites are not expected to be protonated because of their relatively low basicity. We speculate that the protonated form $[\text{HV}_2\text{W}_4\text{O}_{19}]^{3-}$ represents only 30% of the total species present under the conditions specified by the authors. On the NMR timescale, the protonated and non-protonated forms would rapidly interconvert giving a single resonance.

4. Conclusions

We have established a DFT-based strategy to accurately compute and rationalize ^{17}O NMR chemical shifts of polyoxoanions. The lowest deviations between experimental and theoretical values were obtained at OPBE/TZP//PBE/TZ2P (NMR/optimization) level incorporating also solvent and relativistic effects. With this approach and using linear fitting we predict δ values with mean absolute errors ~ 26 ppm for a set of 75 signals.

The paramagnetic contribution of the shielding (σ^P) dominates the ^{17}O chemical shift. It arises from the occupied \rightarrow unoccupied orbital transitions with oxygen contribution promoted by the external magnetic field acting in NMR. The σ^P correlates in general with M–O bond distances. For terminal M=O oxygens, the $\sigma \rightarrow \pi^*$ transition governs the shielding, which also has a linear dependence with the reciprocal of the energy gap. We used the simple MO_4^{n-} anion to clarify the dependence of δ vs. M . Electronegative ions such as V^V , Cr^VI or Ru^VIII , with rather deep $\pi^*(\text{M}-\text{O})$ orbitals, lead to very positive $\delta(^{17}\text{O})$. The less electronegative Nb^V or W^VI ions have the opposite behaviour. The number of metal ions linked to the oxygen atom also affect $\delta(^{17}\text{O})$.

The effect of protonation on POMs has been analysed in detail for hexametalates and $[\text{V}_{10}\text{O}_{28}]^{6-}$. When proton-exchange occurs between chemically similar or equivalent sites, $\delta(^{17}\text{O})$ signals of protonated oxygens move upfield ($\Delta\delta < 0$), whereas the non-protonated ones slightly move downfield ($\Delta\delta > 0$). When a molecule has many similar/equivalent oxygen sites that can accept an itinerant proton, the net effect of protonation is largely dissipated and the changes in $\delta(^{17}\text{O})$ signals could become tiny or even undetectable by NMR as, for instance, the protonated Keggin $[\text{HXW}_{12}\text{O}_{40}]^{n-}$ anion. On the other hand, when a distinctively basic oxygen is present, as the bridging V_2O in $[\text{V}_2\text{W}_4\text{O}_{19}]^{4-}$, the proton gets trapped in one location and a large change (hundreds of ppm) in one ^{17}O NMR signal is observed upon protonation.

Acknowledgements

We thank the Spanish Ministry of Science and Innovation (MICINN) (project CTQ2011-29054-C02-01/BQU) and the DGR of the Generalitat de Catalunya (grant no. 2009SGR462 and the XRQTC). RJE thanks the EPSRC (Grant GR/N65028101) and Newcastle University for funding. XL thanks the Ramón y Cajal program (grant RYC-2008-02493). We also thank CMST COST Action CM1203. A computational grant by the Barcelona Supercomputing Center-Centro Nacional de Supercomputación (BSC-CNS) is acknowledged.

Notes and references

- 1 L. Cronin and A. Müller, Special issue on polyoxometalates chemistry, *Chem. Soc. Rev.*, 2012, 41.
- 2 M. T. Pope and A. Muller, *Angew. Chem., Int. Ed. Engl.*, 1991, **30**, 34–48.
- 3 M. T. Pope, *Heteropoly and Isopoly Oxometalates*, Springer-Verlag, Berlin, 1983.
- 4 A. Müller and S. Roy, in *The Chemistry of Nanomaterials: Synthesis, Properties and Applications*, Wiley-VCH, Weinheim, 2004.
- 5 D.-L. Long, R. Tsunashima and L. Cronin, *Angew. Chem., Int. Ed.*, 2010, **49**, 1736–1758.
- 6 D.-L. Long, E. Burkholder and L. Cronin, *Chem. Soc. Rev.*, 2007, **36**, 105–121.
- 7 B. Hasenknopf, *Front. Biosci.*, 2005, **10**, 275–287.
- 8 M. Nyman and P. C. Burns, *Chem. Soc. Rev.*, 2012, **41**, 7354–7367.
- 9 B. K. Nicholson, C. J. Clark, C. E. Wright, S. G. Telfer and T. Grousto, *Organometallics*, 2011, **30**, 6612–6616.
- 10 L. C. Zhang, R. Clérac, P. Heijboer and W. Schmitt, *Angew. Chem.*, 2012, **124**, 3062–3066.
- 11 E. V. Chubarova, M. H. Dickman, B. Keita, L. Nadjjo, F. Miserque, M. Mifsud, I. W. C. E. Arends and U. Kortz, *Angew. Chem., Int. Ed.*, 2008, **47**, 9542–9546.
- 12 M. Barsukova, N. V. Izarova, R. N. Biboum, B. Keita, L. Nadjjo, V. Ramachandran, N. S. Dalal, N. S. Antonova, J. J. Carbó, J. M. Poblet and U. Kortz, *Chem.–Eur. J.*, 2010, **16**, 9076–9085.
- 13 M. Barsukova-Stuckart, N. V. Izarova, R. Barrett, Z. Wang, J. van Tol, H. W. Kroto, N. S. Dalal, B. Keita, D. Heller and U. Kortz, *Chem.–Eur. J.*, 2012, **18**, 6167–6171.
- 14 M. Pley and M. S. Wickleder, *Angew. Chem., Int. Ed.*, 2004, **43**, 4168–4170.
- 15 M. Pley and M. S. Wickelder, *Z. Naturforsch., B: J. Chem. Sci.*, 2006, **61**, 912–915.
- 16 N. V. Izarova, N. Vankova, T. Heine, R. N. Biboum, B. Keita, L. Nadjjo and U. Kortz, *Angew. Chem., Int. Ed.*, 2010, **49**, 1886–1889.
- 17 I. I. Rabi, J. R. Zacharias, S. Millman and P. Kursch, *Phys. Rev.*, 1938, **53**, 318–327.
- 18 E. M. Purcell, H. C. Torrey and R. V. Pound, *Phys. Rev.*, 1946, **69**, 37–38.
- 19 E. M. Purcell, *Phys. Rev.*, 1949, **76**, 1262–1263.
- 20 I. P. Gerothanassis, *Prog. Nucl. Magn. Reson. Spectrosc.*, 2010, **56**, 95–197.

- 21 I. P. Gerothanassis, *Prog. Nucl. Magn. Reson. Spectrosc.*, 2010, **57**, 1–110.
- 22 J. A. Jackson and H. Taube, *J. Phys. Chem.*, 1965, **69**, 1844–1849.
- 23 B. N. Figgis, R. G. Kidd and R. S. Nyholm, *Can. J. Chem.*, 1965, **43**, 145–153.
- 24 A. D. English, J. P. Jesson, W. G. Klemperer, T. Mamounas, L. Messerle, W. Shum and A. Tramontano, *J. Am. Chem. Soc.*, 1975, **97**, 4785–4786.
- 25 W. G. Klemperer and W. Shum, *J. Am. Chem. Soc.*, 1978, **100**, 4891–4893.
- 26 M. Filowitz, W. G. Klemperer, L. Messerle and W. Shum, *J. Am. Chem. Soc.*, 1976, **98**, 2345–2346.
- 27 M. Filowitz, R. K. C. Ho, W. G. Klemperer and W. Shum, *Inorg. Chem.*, 1979, **18**, 93–103.
- 28 X. López, J. J. Carbó, C. Bo and J. M. Poblet, *Chem. Soc. Rev.*, 2012, **41**, 7537–7571.
- 29 A. Bagno and M. Bonchio, *Chem. Phys. Lett.*, 2000, **317**, 123–128.
- 30 A. Bagno and M. Bonchio, *Angew. Chem., Int. Ed.*, 2005, **44**, 2023–2026.
- 31 A. Bagno, M. Bonchio and J. Autschbach, *Chem.–Eur. J.*, 2006, **12**, 8460–8471.
- 32 J. Gracia, J. M. Poblet, J. A. Fernandez, J. Autschbach and L. P. Kazansky, *Eur. J. Inorg. Chem.*, 2006, 1149–1154.
- 33 J. Gracia, J. M. Poblet, J. Autschbach and L. P. Kazansky, *Eur. J. Inorg. Chem.*, 2006, 1139–1148.
- 34 L. Vilà-Nadal, J. P. Sarasa, A. Rodríguez-Forteza, J. Igual, L. P. Kazansky and J. M. Poblet, *Chem.–Asian J.*, 2010, **5**, 97–104.
- 35 (a) G. te Velde, F. M. Bickelhaupt, S. J. A. van Gisbergen, C. Fonseca Guerra, E. J. Baerends, J. G. Snijders and T. Ziegler, *J. Comput. Chem.*, 2001, **22**, 931–967; (b) C. Fonseca Guerra, J. G. Snijders, G. te Velde and E. J. Baerends, *Theor. Chem. Acc.*, 1998, **99**, 391–403; (c) *ADF2010, SCM*, Theoretical Chemistry, Vrije Universiteit, Amsterdam, The Netherlands, <http://www.scm.com>.
- 36 J. P. Perdew, K. Burke and M. Ernzerhof, *Phys. Rev. Lett.*, 1996, **77**, 3865–3868.
- 37 M. Swart, A. W. Ehlers and K. Lammertsma, *Mol. Phys.*, 2004, **102**, 2467–2474.
- 38 A. D. Becke, *Phys. Rev. A: At., Mol., Opt. Phys.*, 1988, **38**, 3098–3100.
- 39 J. P. Perdew and W. Yue, *Phys. Rev. B*, 1986, **33**, 8800–8802.
- 40 T. W. Keal and D. J. Tozer, *J. Chem. Phys.*, 2003, **119**, 3015–3024.
- 41 J. P. Perdew, J. A. Chevary, S. H. Vosko, K. A. Jackson, M. R. Pederson, D. J. Singh and C. Fiolhais, *Phys. Rev. B: Condens. Matter*, 1992, **46**, 6671–6687.
- 42 M. Swart, M. Solà and F. M. Bickelhaupt, *J. Chem. Phys.*, 2009, **131**, 094103.
- 43 M. Swart, M. Solà and F. M. Bickelhaupt, *J. Comput. Methods Sci. Eng.*, 2009, **9**, 69–77.
- 44 P. J. Stephens, F. J. Devlin, C. F. Chabalowski and M. J. Frisch, *J. Phys. Chem.*, 1994, **98**, 11623–11627.
- 45 S. Grimme, *J. Comput. Chem.*, 2004, **25**, 1463–1473.
- 46 M. Ernzerhof and G. E. Scuseria, *J. Chem. Phys.*, 1999, **110**, 5029–5036.
- 47 E. V. Lenthe, E. J. Baerends and J. G. Snijders, *J. Chem. Phys.*, 1993, **99**, 4597–4610.
- 48 E. V. Lenthe, E. J. Baerends and J. G. Snijders, *J. Chem. Phys.*, 1994, **101**, 9783–9792.
- 49 E. V. Lenthe, A. Ehlers and E. J. Baerends, *J. Chem. Phys.*, 1999, **110**, 8943–8953.
- 50 A. Klamt, *J. Phys. Chem.*, 1995, **99**, 2224–2235.
- 51 A. Klamt, V. Jonas, T. Bürger and J. C. W. Lohrenz, *J. Phys. Chem. A*, 1998, **102**, 5074–5085.
- 52 R. Ditchfield, *Mol. Phys.*, 1974, **27**, 789–807.
- 53 K. Wolinski, J. F. Hinton and P. Pulay, *J. Am. Chem. Soc.*, 1990, **112**, 8251–8260.
- 54 G. Schreckenbach and T. Ziegler, *J. Phys. Chem.*, 1995, **99**, 606–611.
- 55 H. Fukui, *Magn. Reson. Rev.*, 1987, **11**, 205.
- 56 G. Schreckenbach, *Inorg. Chem.*, 2002, **41**, 6560–6572.
- 57 Y. Ruiz-Morales, G. Schreckenbach and T. Ziegler, *J. Phys. Chem.*, 1996, **100**, 3359–3367.
- 58 A. W. Ehlers, Y. Ruiz-Morales, E. J. Baerends and T. Ziegler, *Inorg. Chem.*, 1997, **36**, 5031–5036.
- 59 Y. Ruiz-Morales and T. Ziegler, *J. Phys. Chem. A*, 1998, **102**, 3970–3976.
- 60 J. Autschbach and S. Zheng, *Magn. Reson. Chem.*, 2008, **46**, S45–S55.
- 61 K. Sutter and J. Autschbach, *J. Am. Chem. Soc.*, 2012, **134**, 13374–13385.
- 62 J. F. Zhu, T. Kurahashi, H. Fujii and G. Wu, *Chem. Sci.*, 2012, **3**, 391–397.
- 63 J. Autschbach and S. Zheng, *Magn. Reson. Chem.*, 2006, **44**, 989–1007.
- 64 B. Le Guennic, K. Matsumoto and J. Autschbach, *Magn. Reson. Chem.*, 2004, **42**, S99–S116.
- 65 A. Bagno and R. Bini, *Angew. Chem., Int. Ed.*, 2010, **49**, 1083–1086.
- 66 Y. Zhang, A. Wu, X. Xu and Y. Yan, *Chem. Phys. Lett.*, 2006, **421**, 383–388.
- 67 A. Wu, Y. Zhang, X. Xu and Y. Yan, *J. Comput. Chem.*, 2007, **28**, 2431–2442.
- 68 C. J. Besecker, W. G. Klemperer, D. J. Maltbie and D. A. Wright, *Inorg. Chem.*, 1985, **24**, 1027–1032.
- 69 B. Kandasamy, C. Wills, W. McFarlane, W. Clegg, R. W. Harrington, A. Rodríguez-Forteza, J. M. Poblet, P. G. Bruce and R. J. Errington, *Chem.–Eur. J.*, 2012, **18**, 59–62.
- 70 R. J. Errington, S. S. Petkar, P. S. Middleton, W. McFarlane, W. Clegg, R. A. Coxall and R. W. Harrington, *J. Am. Chem. Soc.*, 2007, **129**, 12181–12196.
- 71 R. J. Errington, S. S. Petkar, P. S. Middleton, W. McFarlane, W. Clegg, R. A. Coxall and R. W. Harrington, *Dalton Trans.*, 2007, 5211–5222.
- 72 M. W. Lodewyk, M. R. Siebert and D. J. Tantillo, *Chem. Rev.*, 2012, **112**, 1839–1862.
- 73 W. Migda and B. Rys, *Magn. Reson. Chem.*, 2004, **42**, 459–466.
- 74 M. Kaupp, V. G. Malkin, O. L. Malkina and D. R. Salahub, *J. Am. Chem. Soc.*, 1995, **117**, 8492.
- 75 M. Kaupp, O. L. Malkina and V. G. Malkin, *J. Chem. Phys.*, 1997, **106**, 9201–9212.

- 76 G. Schreckenbach and T. Ziegler, *Int. J. Quantum Chem.*, 1997, **61**, 899–918.
- 77 B. N. Figgis, R. S. Nyholm and R. G. Kidd, *Proc. R. Soc. London, Ser. A*, 1962, **269**, 469–480.
- 78 W. McFarlane and H. C. E. McFarlane, in *Multinuclear NMR*, ed. J. Mason, Plenum Press, New York, 1987.
- 79 C. Brevard and P. Granger, *J. Chem. Phys.*, 1981, **75**, 4175–4177.
- 80 W. G. Klemperer and W. Shum, *J. Am. Chem. Soc.*, 1977, **99**, 3544–3545.
- 81 V. W. Day, W. G. Klemperer and D. J. Maltbie, *J. Am. Chem. Soc.*, 1987, **109**, 2991–3002.
- 82 A. T. Harrison and O. W. Howarth, *J. Chem. Soc., Dalton Trans.*, 1985, 1953–1957.
- 83 O. W. Howarth, P. Kelly and L. Pettersson, *J. Chem. Soc., Dalton Trans.*, 1990, 81–84.
- 84 J. R. Black, M. Nyman and W. H. Casey, *J. Am. Chem. Soc.*, 2006, **128**, 14712–14720.
- 85 J. Y. Kempf, M. M. Rohmer, J. M. Poblet, C. Bo and M. Benard, *J. Am. Chem. Soc.*, 1992, **114**, 1136–1146.
- 86 A. Dolbecq, A. Guirauden, M. Fourmigue, K. Boubekeur, P. Batail, M.-M. Rohmer, M. Benard, C. Coulon, M. Salle and P. Blanchard, *J. Chem. Soc., Dalton Trans.*, 1999, 1241–1248.
- 87 J. M. Maestre, J. P. Sarasa, C. Bo and J. M. Poblet, *Inorg. Chem.*, 1998, **37**, 3071–3077.
- 88 J. A. Fernández, X. López and J. M. Poblet, *J. Mol. Catal. A: Chem.*, 2007, **262**, 236–242.
- 89 S. Ganapathy, M. Fournier, J. F. Paul, L. Delevoye, M. Guelton and J. P. Amoureux, *J. Am. Chem. Soc.*, 2002, **124**, 7821–7828.
- 90 A. Bagno and G. Scorrano, *Acc. Chem. Res.*, 2000, **33**, 609–616.